

2D hybrid MHD-kinetic electron simulations of an Alfvén wave pulse

P.A. Damiano and A.N. Wright

Mathematical Institute, University of St. Andrews, St. Andrews, Fife,
KY169SS, UK

Abstract.

A 2D hybrid MHD-kinetic model incorporating kinetic electrons is used to simulate a shear Alfvén wave pulse propagating in a constant density plasma and magnetic field. The pulse is rectangular in shape so that the perpendicular and parallel current regions are distinct. Two regimes are considered: the large scale limit where the perpendicular scale length $L_{\perp} \gg \lambda_e$ and the “inertial limit” ($L_{\perp} \leq 10 \lambda_e$). In addition, a potential-current relation is derived from consideration of electron energy in the wave frame. It is found that the parallel electron current is carried by a uniform acceleration of the entire distribution function where larger current is carried by a correspondingly larger displacement. In the inertial limit, the original rectangular shape of the pulse is distorted by a broadening and narrowing in the perpendicular direction at the leading and trailing edges of the pulse respectively as well as by the propagation away from the corners of inertial Alfvén waves with wavelengths $\sim 10 \lambda_e$. In both limits, and in spite of the added structure in the inertial case, the parallel electric field calculated from the derived electrostatic potential reproduces the simulation parallel electric field accurately.

1. Introduction

The link between Alfvén waves (either as pulses or standing modes) and auroral arcs has been well established using both ground based and satellite observations (Xu et al. 1996; Lotko et al. 1998; Chaston et al., 2002; Samson et al. 2003). Associated with these waves are field aligned currents of up to several $\mu A/m^2$ carried primarily by electron beams with energies in the keV range. These beams are accelerated by field aligned electric fields on the order of mV/m in the auroral acceleration region (1-3 R_E altitude).

In the traditional MHD limit $m_e \rightarrow 0$ and there is no parallel electric field to accelerate electrons. However, for straight field lines, with the inclusion of electron mass in the single fluid picture via the generalized ohm's law (Hasegawa, 1976; Wei et al., 1993; Wright et al., 2002), inertial effects become important on the order that the scale length perpendicular to the ambient magnetic field $L_\perp \leq 10 \lambda_e$, where $\lambda_e = \sqrt{m_e/ne^2}$ is the electron inertial length. The MHD approach alone however neglects potentially important effects such as mirror force contributions (Rankin et al., 1999; Rönnmark, 2002) and does not provide any information about the structure and evolution of the electron distribution functions (Wright and Hood, 2003). This has led to approaches that use the Vlasov equation to describe the electron population (Rankin et al, 1999; Wright and Hood, 2003) or more numerical methods using kinetic electrons (Hui and Seyler, 1992; Thompson and Lysak, 1996; Chaston et al., 2000, 2002, 2003; Damiano et al. 2003, 2004).

The 2D model developed by Damiano et al. (2003, 2004) incorporates the full set of cold plasma MHD equations and kinetic electrons using the guiding centre equations as the equations of motion. In this paper we will use the model to consider the case of an

Alfvén wave pulse propagating in a constant density plasma and magnetic field in both the large perpendicular scale length limit ($L_x \gg \lambda_e$) and “inertial regimes” ($L_x \leq 10\lambda_e$). The parameters chosen will be representative of those in the auroral acceleration region. In addition, an electrostatic potential-parallel current density relation is derived using conservation of electron energy arguments in the frame of reference of the pulse and the parallel electric field calculated from the potential is compared directly with that produced from the simulation.

The rest of the paper is broken up into five main sections: Section 2 highlights the hybrid model. Section 3 will present the large perpendicular scale simulation results along with the derivation of the potential-current relation while section 4 summarizes the simulation results for the inertial limit. Section 5 compares the energy densities of the different components and Section 6 has the concluding summary and discussion.

2. Hybrid Model

The 2D cartesian hybrid model used is based on the model summarized in Damiano et al. (2003) with some modifications as discussed in Damiano et al. (2004). It solves explicitly in the x and z directions with the ambient magnetic field B_o directed along the z axis. The limited consideration of a y dimension is allowed by specifying a value for the wave number in the y direction k_y (although $k_y = 0$ is used here).

The model incorporates the full set of the cold plasma MHD equations, but for a toroidal Shear Alfvén wave mode with $k_y = 0$ only the equations for the shear velocity, u_y and perturbed magnetic field b_y are needed given respectively by

$$\frac{\partial u_y}{\partial t} = \frac{B_o}{\mu_o \rho} \left(\frac{\partial b_y}{\partial z} - k_y b_z \right) \quad (1)$$

$$\frac{\partial b_y}{\partial t} = \frac{\partial E_z}{\partial x} - \frac{\partial E_x}{\partial z}. \quad (2)$$

For the electrons, gyroradius effects are negligible for magnetospheric scales and so the guiding center equations

$$\frac{dv_e}{dt} = -\frac{e}{m_e} E_z \quad (3)$$

$$\frac{dr_{gz}}{dt} = v_e \quad (4)$$

are used as the equations of motion for the electrons parallel to the ambient magnetic field where r_{gz} is the parallel component of the guiding centre and v_e is the parallel component of the electron guiding centre velocity. The closure between the MHD equations and the kinetic electrons is obtained via the parallel electric field given by a modification of the generalized ohm's law (Damiano et al., 2004, Hui and Seyler, 1992)

$$\frac{\partial^2 E_z}{\partial x^2} - \frac{1}{\lambda_e^2} E_z = \frac{\partial}{\partial z} \left(\frac{\partial E_x}{\partial x} \right) + \mu_o e \frac{\partial}{\partial z} \sum_i v_{e_i}^2 S(\vec{x}, \vec{x}_i) - \frac{1}{\epsilon_o} \frac{\partial}{\partial z} \left(\int_0^t dt \left(\frac{\partial j_x}{\partial x} + \frac{\partial j_e}{\partial z} \right) \right) \quad (5)$$

where $E_x = -u_y B_o$ is the perpendicular electric field from the ideal MHD approximation, $\lambda_e^2 = m_e / (\mu_o n e^2)$ is the electron inertial length, $j_e = -e \sum_i v_{e_i} S(\vec{x}, \vec{x}_i)$ is the parallel electron current and $S(\vec{x}, \vec{x}_i)$ is the particle shape function (Birdsall and Langdon, 1991). The second term on the right-hand-side is related to the second moment of the electron distribution function and the last term to the quasineutrality of the plasma. The last term arises since quasineutrality is not directly assumed in the model and there is an electric field contribution when $\nabla \cdot \vec{j} \neq 0$. The simulations are quasineutral as a consequence

of the system evolution rather than as an initial assumption (see Damiano et al., 2004). Throughout the simulation, $\rho = nm_i$, V_A and λ_e were continually adjusted consistently with variations in the electron number density, n .

Both the MHD and guiding centre equations are solved using a predictor-corrector method (see Damiano et al. 2003, 2004) and the MHD equations are solved on a set rectangular grid, while the electrons are free to move anywhere in the 2D space. The grid has constant, but different spacing in each direction. The electron density, current and pressure are interpolated to the grid points using biquadratic spline interpolation (Birdsall and Landgon, 1991) represented above by the particle shape function $S(\vec{x}, \vec{x}_i)$ where \vec{x}_i is position of the i^{th} electron and \vec{x} is the grid cell position. The field values are interpolated to the particle positions using the same method.

The magnetic field was normalized by the ambient magnetic field B_o , length by an earth radius $L_N = R_E$, density by the ambient plasma density $\rho_N = nm_p$ (where n is the plasma number density) and velocity by the ambient Alfvén speed $V_N = \sqrt{B_o/(\mu_o\rho_N)}$. Using these definitions, time, electric field and current density were normalized respectively as $t_N = L_N/V_A$, $E_N = V_NB_o$ and $j_N = B_o/(\mu_oL_N)$. For the simulations presented here, the parameters were chosen to be roughly consistent with the auroral acceleration region at an altitude of 1-3 R_E with a constant ambient magnetic field of $B_o = 5000$ nT and a constant number density of $n = 1$ cm^{-3} . The simulation electrons were loaded with constant (but different) spacing in the x and z directions. Each electron is a “superparticle” representative of many electrons. The scaling is determined by the ratio of the ambient plasma density and the simulation electron number density (Damiano et al.,

2003). The velocities were assigned to the electrons using a 1D Maxwellian as a probability distribution function

$$f(v_e) \propto e^{-m_e v_e^2 / 2kT} \quad (6)$$

where $kT = 100$ eV was used.

The system was perturbed by introducing a pulse perturbation in u_y in the centre of the simulation grid. To be consistent with values commonly seen in ULF wave phenomena, an initial value of u_y consistent with a perturbed magnetic field value of $b_y = 100$ nT was chosen using the standard Alfvén-Walén (Alfvén 1942; Walén, 1944; Cross, 1988) relation

$$u_y = \frac{V_A b_y}{B_o}. \quad (7)$$

The left hand panel of Fig. 1 illustrates a contour plot of the initial pulse perturbation for u_y while the right hand panel illustrates the envelope found from a slice in the x direction, where the L_x is the width of the region of variation at either edge of the pulse. This edge region was done using a half period cosine function. A slice in the z direction would illustrate an identical geometry, but with the parameter L_z . The general (x,z) variation is found by taking the product of the normalized envelopes in x and z multiplied by the amplitude value of u_y determined from the Walén relation above. This idealized shape was chosen to create a current loop around the outside of the pulse region and clearly distinguish the perpendicular current regions carried by ions and the parallel current regions carried by electrons.

The values of L_x were chosen to represent two distinct limits: the large perpendicular scale length limit ($L_x \gg \lambda_e$) where electron mass effects are negligible and the “inertial limit” where they are important ($L_x \leq 10\lambda_e$). For the number density $n = 1.0 \text{ cm}^{-3}$, $\lambda_e = 5.3 \text{ km}$ and so the two cases $L_x = 100 \text{ km}$ ($L_x = 18.86\lambda_e$) and $L_x = 25 \text{ km}$ ($L_x = 4.72\lambda_e$) were chosen. In both cases, the value of L_z was chosen to be an R_E to roughly correspond to the parallel scale in the auroral acceleration region (although this choice is not of critical importance). Fig. 1 illustrates the initial perturbation for $L_x = 100 \text{ km}$. In the z direction, the grid extends from $z=0$ to 16 in nondimensional units and 200 grid points are used. The large range is chosen to give the pulse sufficient distance to propagate before reaching the edges (although periodic boundary conditions are used in this direction). In the x direction, the grid range is from $x=0$ to 0.1 for $L_x = 100 \text{ km}$ and from 0 to 0.04 for $L_x = 25 \text{ km}$. In both cases 150 grid points were used and the boundary conditions were open ($\partial/\partial x = 0$), although this was not of importance as the waves do not reach the boundaries during the simulation. For both limits, the time step was 2.5×10^{-5} and the number of simulation electrons used was 15×10^6 (1000 equally spaced initial particle positions in the x direction and 15000 in z , see Damiano et al., 2003). With these parameters, the percentage change in energy over the length of the run (see Section 5) was $5 \times 10^{-2}\%$ illustrating that energy was well conserved. A convergence test was also made by doing a second run for the $L_x = 25 \text{ km}$ case with twice the number of grid points, half the time step and using 24×10^6 simulation electrons. The velocity field u_y was compared with the values from the original run at the end of the simulation ($t=0.009$, see later) using the quantity

$$\frac{\sum_i |u'_{y_i} - u_{y_i}|}{\sum_i |u'_{y_i} + u_{y_i}|/2} \quad (8)$$

to give an estimate of the change in u_y between the two runs. The primed values are from the simulation with increased resolution and the summation is over the common grid points in the two runs. This error in the fields by this measure was 5% indicating good convergence.

3. Simulation in the large scale limit ($L_x = 100 \text{ km}$)

The pulse perturbation introduced at $t=0$ splits up into two identical pulses propagating away from each other toward the upper and lower z boundaries with speeds V_A and $-V_A$ respectively. For the simulations presented in this section, we concentrate on the pulse propagating toward the lower end of the grid, specifically for a snapshot at $t = 0.009$. Fig. 2 illustrates contours of u_y and b_y . Both have similar magnitudes which is to be expected from the Walén relation and they propagate maintaining the same shape as the initial perturbation with only some minor modifications at the corners. The fact that two identical pulses have split away from the initial pulse is evident in that the magnitude in this case is half of the initial value.

Fig. 3 illustrates contour plots of the perpendicular current j_x and parallel current j_e . As expected, they form a current ring around the pulse with perpendicular currents along the top and bottom edges ($j_x = -\frac{\partial b_y}{\partial z}$) closed by parallel electron current along the left and right edges ($j_e = j_z = \frac{\partial b_y}{\partial x}$). Fig. 4 illustrates a slice along the middle of the right hand negative current region at $x = 0.072$ in combination with a series of plots of the distribution function. The plot is the instantaneous slice at $t = 0.009$. However, it can

also be pictured as a series of time slices for an observer sitting at $z=1$ where the ambient background distribution function is accelerated just as the leading edge of the pulse begins to pass (panel for $z=2$). This acceleration is manifested by a slight displacement of the entire distribution function to the right. This is consistent with the negative current as is evident from the definition $j_e = -ne\langle v_e \rangle$. As the constant current region passes, the distribution function maintains a constant displacement (panels for $z=3$ and 4) and then as the trailing edge of the pulse passes, the distribution function is decelerated back to the background maxwellian (last two panels). This implies that there must be regions of nonzero parallel electric field centered around $z=2$ and $z=5$ to accelerate and decelerate the electron population respectively. Exactly such a profile is shown in the left hand panel of Fig. 5 which illustrates the parallel electric field directly from the simulation at $t = 0.009$. We will return to a discussion of the right hand panel shortly.

3.1. Electrostatic Potential-Current Relation

For consideration of the energy with respect to the electrons, it is convenient to move to the frame of reference moving with the pulse (wave frame) where $\partial/\partial t = 0$ and so the system is to first order quasistatic. Considering again the pulse propagating toward $z = 0$ with speed $-V_A$, the velocity of an electron measured in the frame of reference of the pulse is given by

$$v_{ew} = v_e + V_A \tag{9}$$

where v_e is the velocity of the electron in the plasma frame. The conservation of energy for the electron in the wave frame (in the absence of converging magnetic field) is then given by

$$\frac{1}{2}m_e v_{ew}^2 - e\phi = U_e \quad (10)$$

where ϕ is the electrostatic potential and U_e is the electron's total energy in the wave frame. For a population of cold electrons with number density n , this can be expressed as

$$\frac{1}{2}\langle nm_e v_{ew}^2 \rangle - ne\phi = W \quad (11)$$

where the brackets are indicative of average and W is the total energy density. Using equation (9) this becomes

$$\frac{1}{2}nm_e(V_A^2 + 2\langle v_e \rangle V_A) - ne\phi = W \quad (12)$$

where $\langle v_e \rangle = -j_e/ne$ and the term $v_e^2 V_A^2$ was neglected since $v_e \ll V_A$. Far from the pulse, $j_e = 0$ and $\phi = 0$ which gives

$$W = \frac{1}{2}nm_e V_A^2. \quad (13)$$

Since pressure effects are negligible in a cold plasma, the energy density is conserved and

$$\frac{1}{2}nm_e(V_A^2 + 2\langle v_e \rangle V_A) - ne\phi = \frac{1}{2}nm_e V_A^2. \quad (14)$$

Substituting in for $\langle v_e \rangle$ in terms of j_e , this simplifies to

$$\phi = -\frac{m_e j_e V_A}{n e^2}. \quad (15)$$

Using the parallel current from Fig. 3 and the corresponding profiles for V_A and n from the simulation, the profile of the electrostatic potential calculated using expression (15) is illustrated in Fig. 6. Not surprisingly, it exhibits the same basic profile as the field aligned current density. Now, calculating the parallel electric field from the potential using

$$E_z = -\frac{\partial \phi}{\partial z} \quad (16)$$

the results are displayed in the right panel in Fig (5). As is evident, this result agrees very well with the parallel electric field taken directly from the simulation (plotted in the left hand panel) illustrating that the electrostatic potential offers a good instantaneous picture of the parallel electric field.

4. Simulation in the inertial limit ($L_x = 25 \text{ km}$)

For the following simulation, $L_x = 25 \text{ km}$ was used and the radial dimensions of the grid were reset to $0 \leq x \leq 0.04$ in nondimensional units. All other parameters remained the same. Fig. 7 illustrates the parallel current at $t = 0.009$. As is evident, the contours are much more complicated than illustrated in Fig. 3. Two main features are manifested. The first is a broadening of the pulse width at the leading edge and a narrowing at the trailing edge with the entire pulse length being greater than that exhibited for large L_x . The second feature is the appearance of small amplitude waves propagating away from the pulse edges in the perpendicular direction. The small contour value of 50 (compared to

the peak value of 1200) has been chosen to bring out these wave features which are much more prominent in the contours of the parallel electric field to be discussed below. The smaller value of L_x implies that the parallel current should be larger and this is evident in Fig. 8 which is a slice along the center of the right hand parallel current region at $x = 0.029$ along with the distribution functions at the points indicated. As is evident, the larger parallel current is carried by a larger displacement of the electron distribution function.

Fig. 9 illustrates the parallel electric field at $t = 0.009$ from both the simulation (left panel) and the electrostatic potential (right panel) calculated in the same way as discussed in the previous section. As with the current, the parallel electric field exhibits a broadening at the leading edges and a narrowing at the trailing edges along with the wave structure propagating away from the corners of the pulse in the perpendicular direction. Since we are in the limit $L_x \leq \lambda_e$, the inertial Alfvén wave dispersion relation applies and these are inertial Alfvén waves. A better picture is illustrated in the plots at the bottom of the panels in Fig. 9 which are slices of E_z as a function of x at $z = 2.96$ for both cases. The wavelength of the waves is approximately 50 km which is on the expected order of $10 \lambda_e$ (where $\lambda_e = 5.3 \text{ km}$) where electron inertial effects become important. In addition, comparison of Figures. 5 and 9 illustrates the corresponding larger electric field needed to accelerate the electrons in the latter case.

The fact that the quasistatic approximation still works in this regime is not surprising when one examines the electron and Alfvén time scales in the wave frame. For an electron, the relevant time scale is simply the time scale needed to cross the region L_z and as the electrons are moving with approximately the Alfvén speed in the wave frame, the time

scale $\tau_e = L_z/V_A = 0.002$ in nondimensional units. On the other hand, the Alfvén frequency in the wave frame is

$$\omega_{Aw} = \omega_{Ap} - k_z V_A = \frac{k_z V_A}{\sqrt{1 + k_x^2 \lambda_e^2}} - k_z V_A. \quad (17)$$

where ω_{Ap} is the inertial Alfvén wave frequency in the plasma frame. As is evident, in the MHD limit ($m_e \rightarrow 0$), $\omega_{Aw} = 0$ in this frame of reference which is approximately the case in the large scale limit. This implies $\tau_{Aw} = \frac{2\pi}{|\omega_{Aw}|} = \infty$ and so $\partial/\partial t$ is exactly 0. Therefore an observer moving with speed $-V_A$ would see no changes in the field values. In the inertial limit though, ω_{Aw} has a nonzero value and τ_{Aw} is finite and an observer would see changes in this fields on this time scale. Considering the dominant mode $k_x = 2\pi/L_x$, Fig. 10 plots the ratio of the electron transit time to the the Alfvén wave period as a function of L_x in units of λ_e . As L_x gets smaller the Alfvén period approaches the electron transit time and the quasistatic approximation breaks down. However, for the minimum parameters used here ($L_x \approx 5\lambda_e$), τ_{Aw} is approximately three times larger than τ_e and so it is not surprising that the quasistatic approximation was still very good; i.e. the wave fields do not change much during the electron transit. That the approximation breaks down for much smaller L_x was confirmed by a test run with $L_x \approx 2\lambda_e$, where the structure of parallel electric field determined from the potential diverged fairly significantly from the simulation field.

It should be noted that the true wave frame for the pulse is not moving with $-V_A$, but with the phase speed of the inertial Alfvén wave. For the large scale limit, this is a very good approximation which progressively gets worse as L_x gets smaller. It is not possible to transform to an inertial Alfvén wave frame, since the different k_x modes present will

propagate in z at slightly different speeds - as evidenced by the evolved structure in Fig. 7. However, the expression derived in the frame moving with the Alfvén speed reconstructed E_z very accurately for the perpendicular scales of interest and suggests the error is small.

5. Energy

The 2-D energy density (energy density per unit y) of the hybrid MHD-kinetic system in the plasma frame and for periodic boundary conditions is given in nondimensional units by (Damiano et al., 2004)

$$\frac{1}{2}\rho u_y^2 + \frac{b_y^2}{2} + W_e \quad (18)$$

where W_e is the kinetic energy density of the electrons (where the kinetic energy of an electron is $1/2m_e v_e^2$). Fig 11 illustrates a slice at $z = 2.96$ of the individual energy density terms as a function of x for $L_x = 100 \text{ km}$ in the top right panel and $L_x = 25 \text{ km}$ in the top left panel. Both plots are for $t = 0.009$. The densities are normalized so that the maximum energy density in u_y is 1. As is evident, there is relatively little energy residing in the electrons in the large perpendicular scale limit but for the inertial case, they account for a more significant portion. In Wright et al. (2003) it was shown that the ratio of the electron energy density to the magnetic energy in the two fluid picture can be expressed in terms of λ_e and L_x as

$$\frac{1/2nm_e\langle v_e \rangle^2}{b_y^2/2} \approx \frac{\lambda_e^2}{L_x^2}. \quad (19)$$

Using $\lambda_e = 5.3 \text{ km}$ and $L_x = 100 \text{ km}$, the ratio is approximately 0.045. This is consistent with the maximum values illustrated in the right top panel of Fig 11. The two fluid

approximation works well here because of the large displacement of the entire distribution function. The shifting of the peak electrons with original velocity close to zero adds the largest contribution to the energy in the displaced picture and consequently, the thermal energy residing in the width of the distribution (which is not incorporated in (19)) is of secondary importance. This is emphasized by the plot in the bottom panel of the electron energy density for the original simulation and one with $kT = 10 \text{ eV}$. In the $kT = 100 \text{ eV}$ case, there is a larger background energy density which would correspond to the thermal energy of the ambient distribution function, but it is still significantly less than the energy density associated with the shift in the distribution function. Also, the magnitude of the rise in energy density relative to the background is approximately the same in both cases, as expected.

In Fig. 12 the total energy is plotted as a function of time in the inertial case illustrating that total energy is nicely conserved for the MHD-kinetic system as well. The gradual drop in the energy in u_y and the corresponding increase in the energy in b_y for $t \leq 0.003$ is due to the splitting of the initial perturbation which only had energy in u_y . In the large scale limit, almost all the energy is split equally between the u_y and b_y modes satisfying the Alfvén-Walén relation discussed previously, with a slight increase in the electron energy as the pulses separate and the currents emerge.

6. Summary and Discussion

We have used the 2D hybrid MHD-kinetic model of Damiano et al. (2003, 2004) to consider the case of a rectangular shaped Alfvén wave pulse propagating in a constant density plasma and magnetic field in both the large perpendicular scale and inertial limits. In addition, we have derived a relation between the electrostatic potential and the parallel

current density based on conservation of energy arguments in the frame of reference of the pulse and a comparison was made between the parallel electric field determined from this potential and that produced directly from the model.

In the limit of large perpendicular scale length ($L_x = 100 \text{ km}$) the pulse propagates with speed V_A and maintains its original geometry with slight modifications at the corners. The geometry of the pulse results in a clear separation of the perpendicular and parallel current regions around the edges of the pulse. Nonzero parallel electric field values appear at leading and trailing corners to accelerate the electrons to carry the parallel current along the edge and then decelerate them when the current edge region has passed. For the parameters considered here, the entire distribution function is accelerated to carry the current. In this limit, as would be expected, the largest portion of the energy is by far concentrated in the u_y and b_y components with a small amount residing in the electrons.

In the “inertial limit” ($L_x = 25 \text{ km}$), the above simple picture becomes somewhat more complicated. The parallel current regions becomes more elongated in the parallel direction than in the large scale limit and are broadened at the leading edge and narrowed at the trailing edge. In addition, small amplitude inertial Alfvén waves with wavelengths $\sim 10 \lambda_e$ are seen to be propagating away from the leading and trailing corners of the pulse. These features are more clearly visible in the profile of the parallel electric field where in addition to the inertial scale structure, the oval profiles seen at the corners of the pulse in the large scale limit, broaden at their respective leading edges. Interestingly though, the parallel electric field determined from the derived quasistatic potential-current relation still does a very good job of reproducing the simulation parallel electric field (as was the case in the large scale limit). The smaller value of L_x also results in a stronger parallel

current which is carried by a larger displacement of the electron distribution function. This large displacement means the energy stored in the electrons becomes significant and the almost exact equipartition of energy between the u_y and b_y components evident in the MHD limit breaks down. The proportion of energy residing in the electrons is in agreement with predicted by the relation derived in Wright et al. (2003) using two-fluid theory.

Although this pulse simulation is not meant to be representative of ULF waves in the auroral acceleration region, the choice of parameters was designed to produce relatively realistic parallel current densities and spatial scales. In the $L_x = 100 \text{ km}$ case, the maximum value of j_e is $\sim 0.6 \mu\text{A}/\text{m}^2$ and for $L_x = 25 \text{ km}$ the result was $j_e \sim 2 \mu\text{A}/\text{m}^2$. The energies of the electrons in the central shifted peaks of the distributions carrying this current were on the order of 50 eV and 300 eV respectively and the corresponding peak parallel electric fields were $\sim 0.6 \text{ mV}/\text{m}$ and $\sim 1 \text{ mV}/\text{m}$ respectively. These values for E_z are also of the order of magnitude that are expected for the acceleration of electrons by ULF waves.

In summary, the work presents a clear and complete examination of what is happening during the propagation of an Alfvén pulse in the hybrid picture. It illustrates the effectiveness of the electrostatic potential to provide an accurate instantaneous picture of the parallel electric field in a wave frame for which the fields are approximately steady. Also, although the geometry was idealized to clearly separate perpendicular and parallel current regions, such geometries can occur naturally in the shearing of magnetic field lines in plasma flow past a conducting body, such as in the wake of flow past Io (Wright

and Southwood, 1987) or flow in the earth's magnetosheath relative to the conducting ionosphere of the earth (Wright, 1996).

Acknowledgments. PAD is funded by a PPARC grant. Simulations were conducted using the PPARC funded St. Andrews Maths Cluster.

References

- Alfvén H., On the existence of electromagnetic-hydromagnetic waves *Ark. Mat. Astron. Fys.* 29B(2), 1942.
- Birdsall, C.K., and A.B. Langdon, Plasma Physics via Computer Simulation, IOP Publishing, 1991.
- Cross, Rodney, An Introduction to Alfvén Waves, IOP Publishing, 1988.
- Chaston, C.C., C.W. Carlson, R.E. Ergun, and J.P. McFadden, Alfvén waves, density cavities and electron acceleration observed from the FAST spacecraft *Phys. Scr. T84*, 64, 2000.
- Chaston C.C., J.W. Bonnell, L.M. Peticolas, C.W. Carlson, J.P. McFadden and R.E. Ergun, Driven Alfvén waves and electron acceleration, *Geophys. Res. Lett.*, 29(11), 10.1029/2001GL013842, 2002.
- Chaston, C.C., J.W. Bonnell, C.W. Carlson, J.P. McFadden, R.E. Ergun, and R.J. Strangeway, *Properties of small-scale Alfvén waves and accelerated electrons from FAST*, 108(A4), 8003, doi:10.1029/2002JA009420, 2003.
- Damiano, Peter A., R.D. Sydora, and J.C. Samson, Hybrid magnetohydrodynamic-kinetic model of a standing shear Alfvén waves *J. of Plasma Phys.*, 69, 277, 2003.

- Damiano, P.A., A.N. Wright, R.D. Sydora, and J.C. Samson, Quasineutrality and closure schemes in hybrid MHD-kinetic models of standing shear Alfvén waves *Submitted to Physics of Plasmas*, 2004.
- Hasegawa, Akira, Particle acceleration by MHD surface waves and formation of aurora, *J. of Geophys. Res.*, *81*, 5083, 1976.
- Hui, C.-H., and C.E. Seyler, Electron acceleration by Alfvén waves in the magnetosphere, *J. Geophys. Res.*, *97*, 3953, 1992.
- Lotko, W., A.V. Streltsov, and C.W. Carlson, Discrete auroral arcs, electrostatic shocks and suprathermal electrons powered by dispersive, anomalously resistive field line resonances, *Geophys. Res. Lett.* *25*, 4449, 1998.
- Rönnmark, K., Auroral current-voltage relation, *J. Geophys. Res.*, *107*, 1430, doi:10.1029/2002JA009294, 2002.
- Samson, J.C., R. Rankin and V.T. Tikhonchuk, Optical signatures of auroral arcs produced by field line resonances: comparison with satellite observations and modeling *Annales Geophysicae*, *21*, 1, 2003.
- Thompson, B.J., and R.L. Lysak, Electron acceleration by inertial Alfvén waves, *J. of Geophys. Res.*, *101*, 5359, 1996.
- Walén, C., On the theory of sunspots, *Ark. Mat. Astron. fys.* *30A(15)*, 1944.
- Wei, C.Q., J.C. Samson, R. Rankin and P. Frycz, Electron inertial effects on geomagnetic field line resonances, *J. of Geophys. Res.*, *99*, 11265, 1994.
- Wright, A.N. and D.J. Southwood, Stationary Alfvénic structures, *J. Geophys. Res.*, *92*, 1167, 1987.

- Wright, A.N., Transfer of magnetosheath momentum and energy to the ionosphere along open field lines, *J. Geophys. Res.* *101*, 13,169, 1996.
- Wright, A.N., W. Allan, M.R. Ruderman and R.C. Elphic, The dynamics of current carriers in standing Alfvén waves: Parallel electric fields in the auroral acceleration region, *J. Geophys. Res.* *107*, 10.1029/2001JA900168, 2002.
- Wright, A.N. and A.W. Hood, Field-aligned electron acceleration in Alfvén waves, *J. Geophys. Res.* *108(A3)*, 1135, doi:10.1029/2002JA009551, 2003.
- Wright, Andrew N., W. Allan and Peter A. Damiano, Alfvén wave dissipation via electron energization *Geophys. Res. Lett.*, *30(16)*, 1847, doi:10.1029/2003GL017605, 2003.
- Xu, B-L., J.C. Samson, W.W. Liu, F. Creutzberg, and T.J. Hughes, Observations of optical aurora modulated by resonant Alfvén waves, *J. Geophys. Res.*, *98*, 11531, 1993.

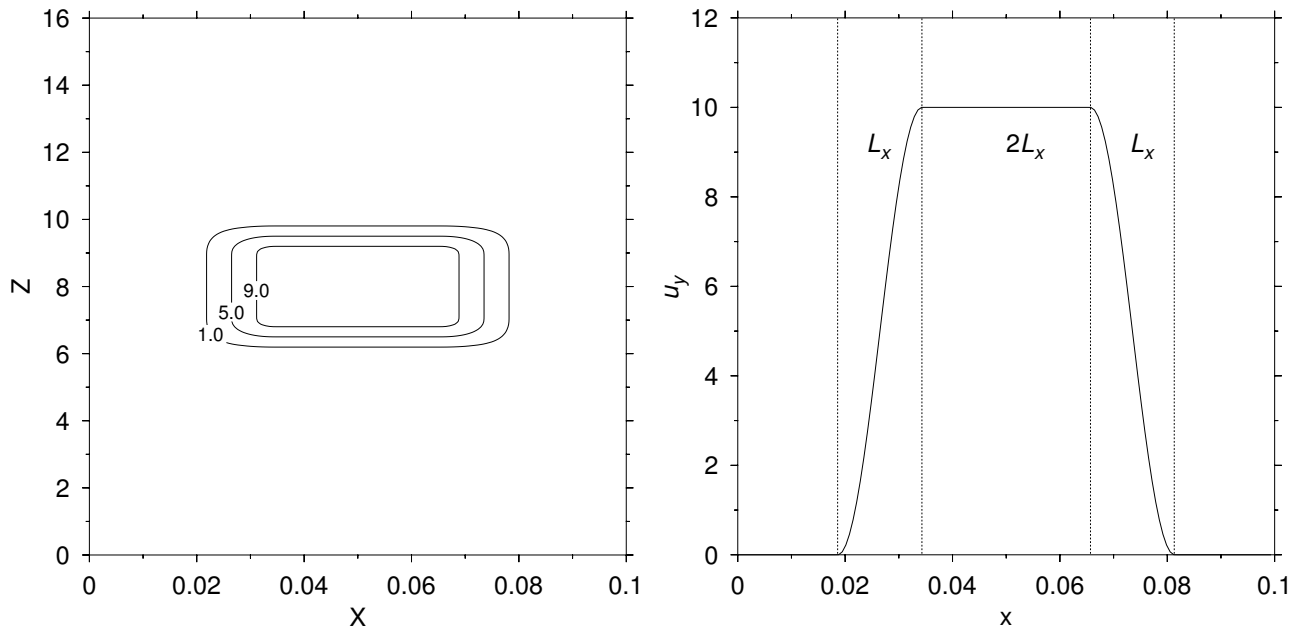


Figure 1. Left: Contours of the initial shear velocity perturbation u_y at $t = 0$ for $L_x = 100$ km . Right: Slice in x along the center of the velocity perturbation.

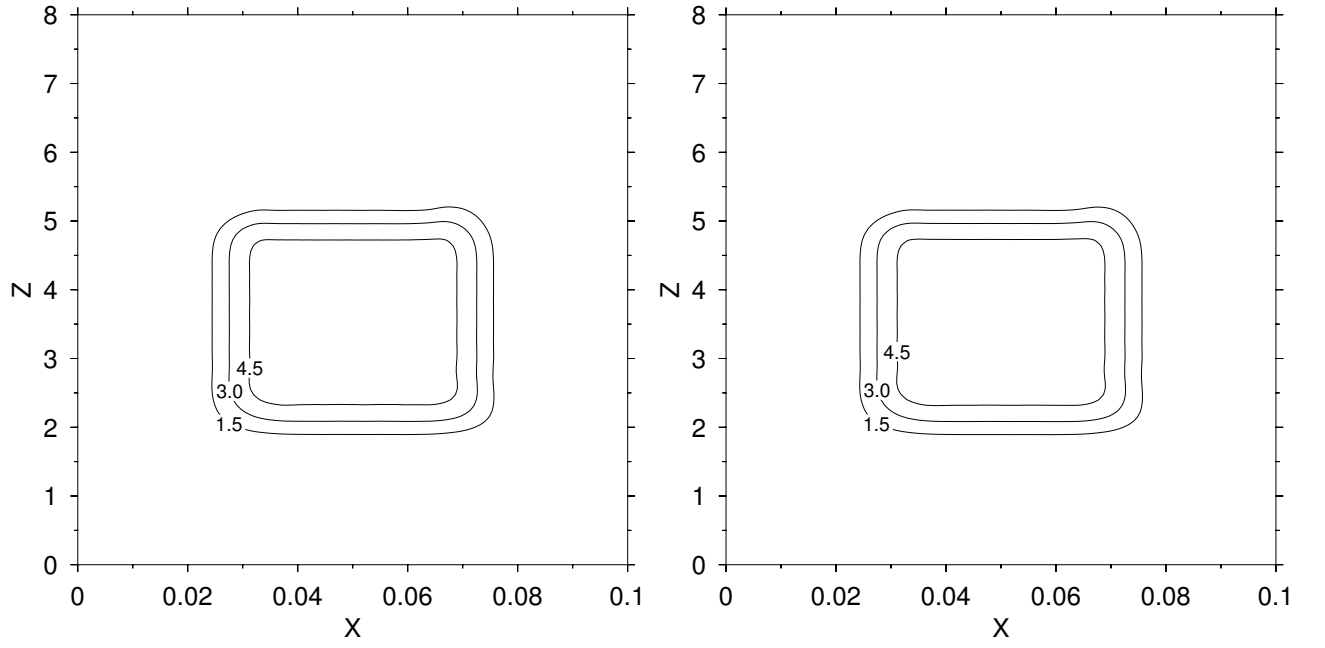


Figure 2. Contours of u_y (left) and b_y (right) at $t = 0.009$ for the $L_x = 100$ km simulation.

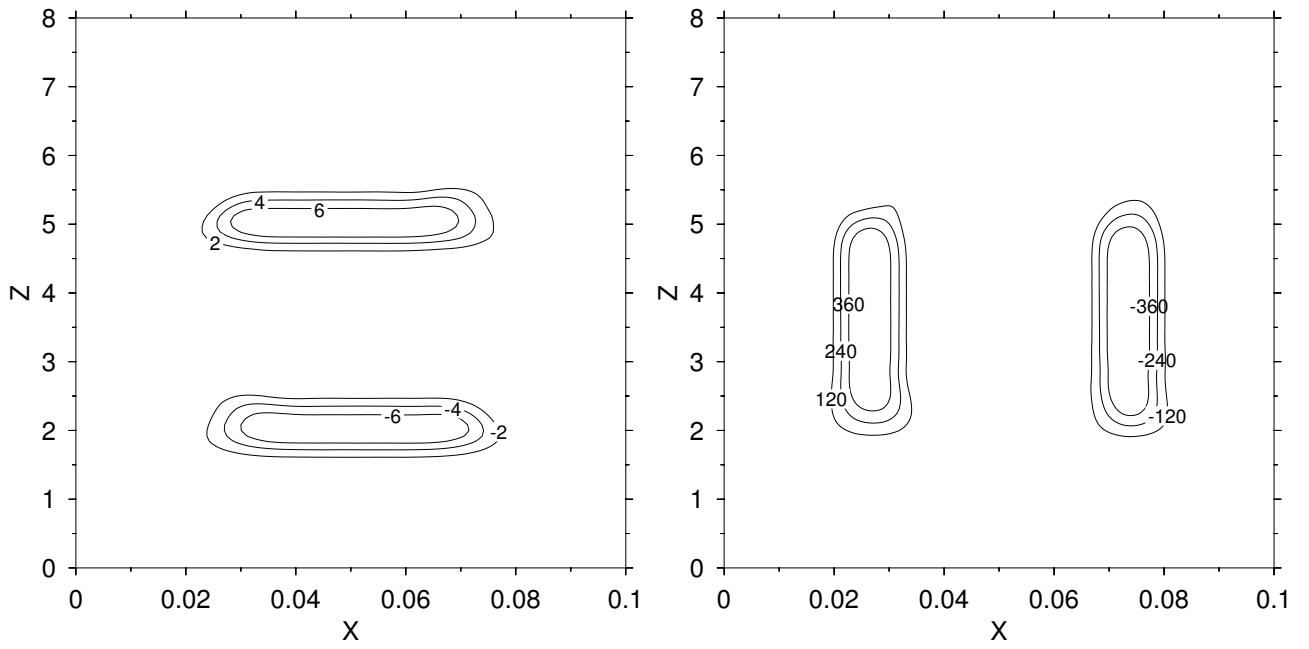


Figure 3. Contours of perpendicular current density j_x (left) and parallel current density j_e (right) at $t = 0.009$ for the $L_x = 100$ km simulation.

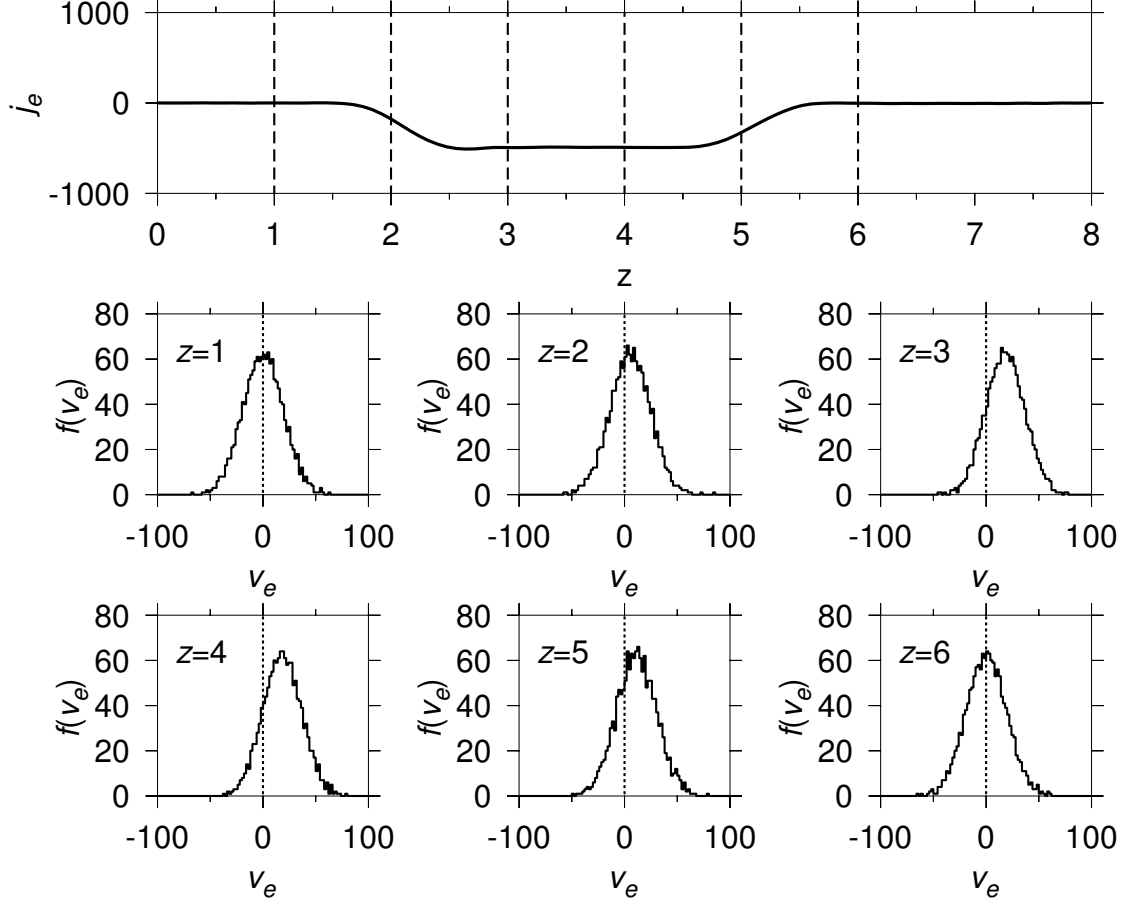


Figure 4. Top: Slice of parallel current density as a function of z at $x = 0.725$ and $t = 0.009$. Bottom: The corresponding electron distribution functions at the points indicated. The distribution functions were calculated using electrons in the z grid interval closest to the indicated points and within $0.072 \leq x \leq 0.074$.

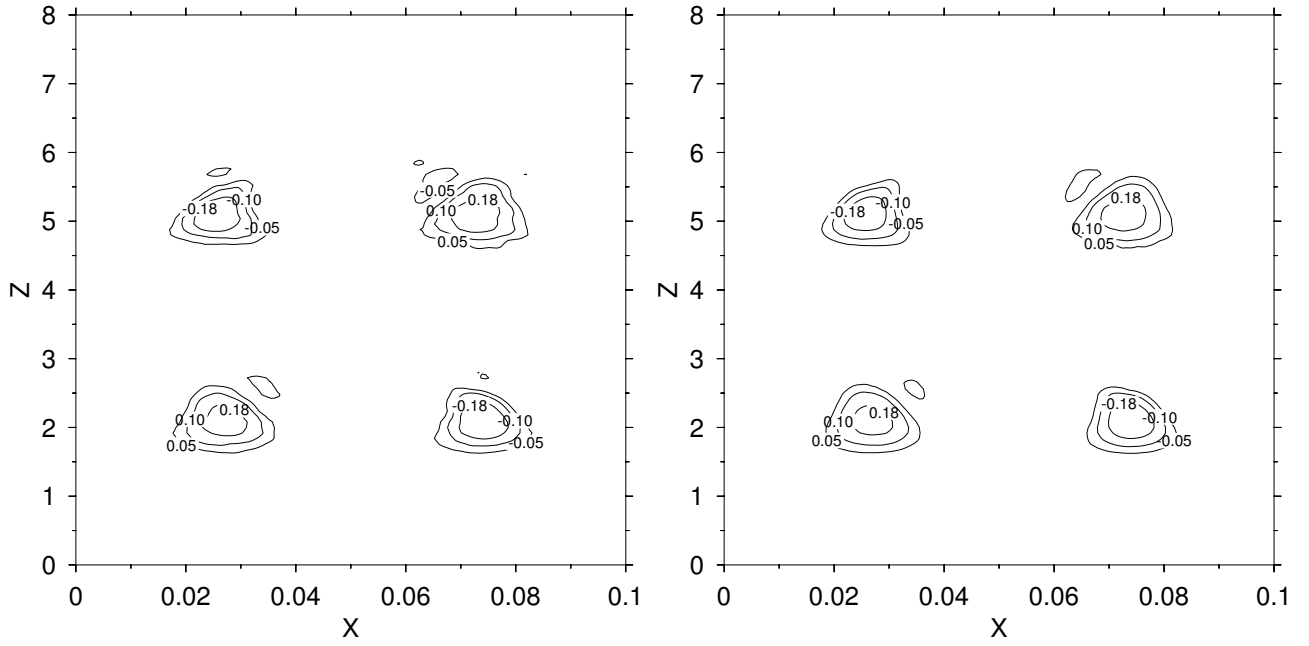


Figure 5. Contours of parallel electric field from the simulation (left) and that calculated from the potential ϕ (right) at $t = 0.009$ for the $L_x = 100$ km case.

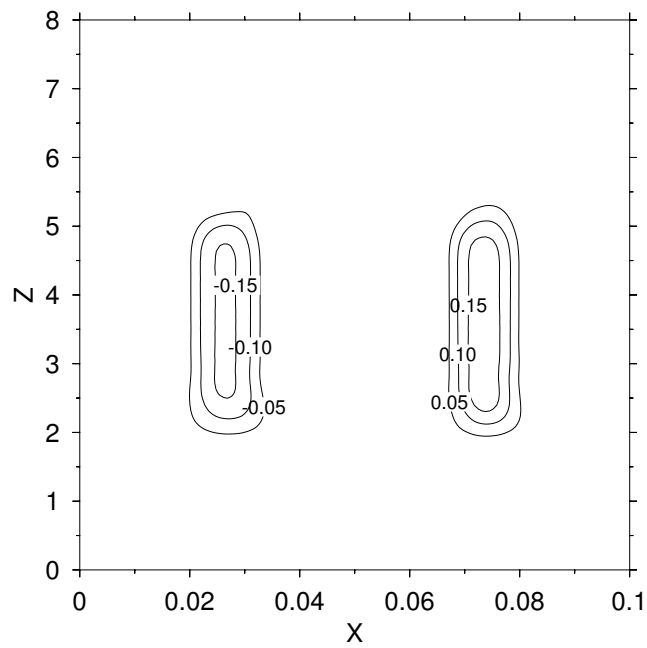


Figure 6. Contours of electrostatic potential ϕ calculated from expression (15) using the parallel current illustrated in Fig. (3)

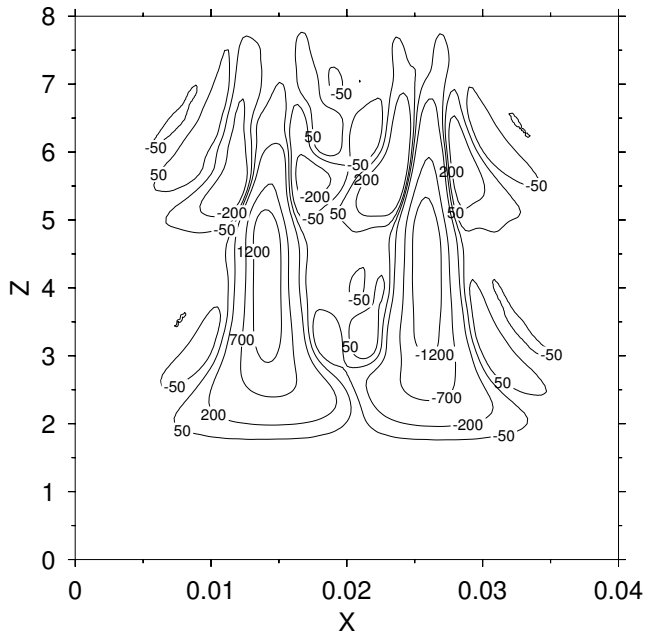


Figure 7. Contours of parallel electron current, j_e , at $t = 0.009$ for the $L_x = 25$ km simulation.

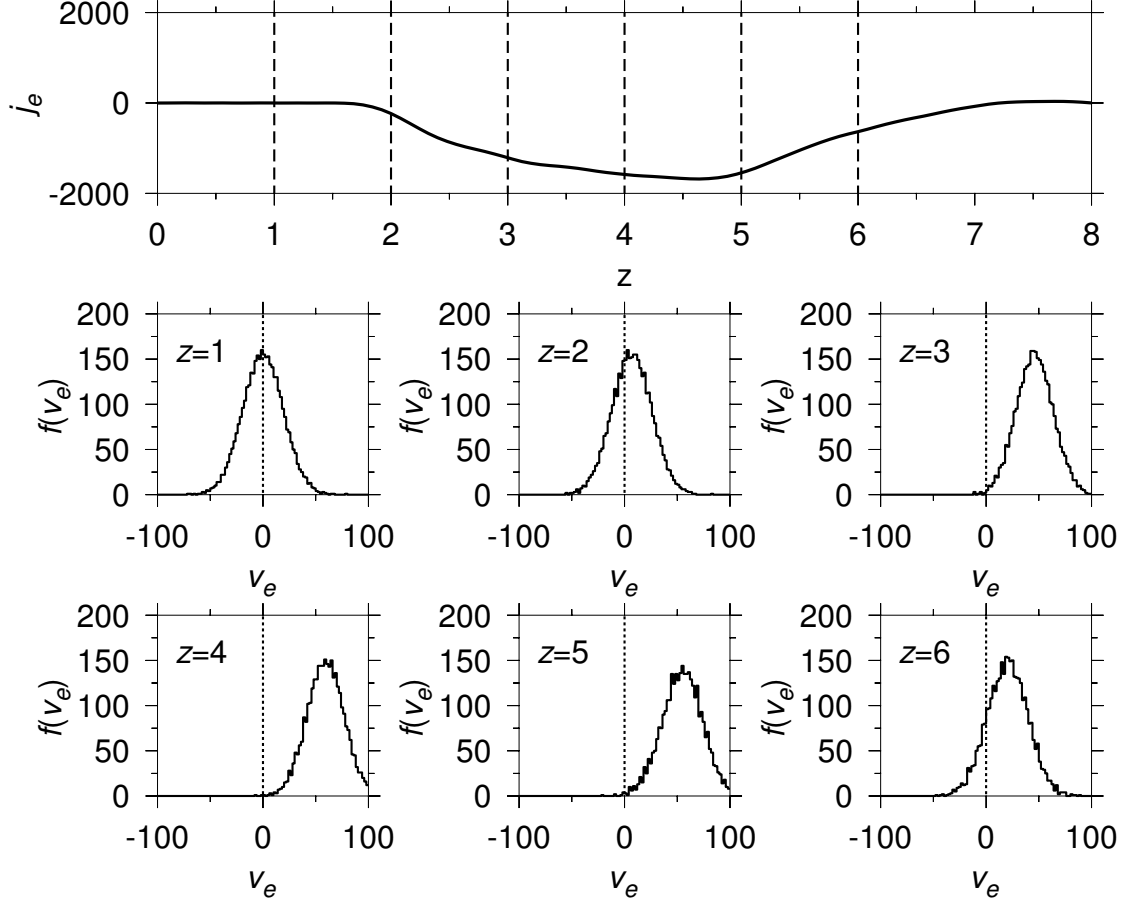


Figure 8. Top: Slice of parallel current density as a function of z at $x = 0.026$ and $t = 0.009$ for the $L_x = 25$ km case. Bottom: The corresponding electron distribution functions at the points indicated. The distribution functions were calculated using electrons in the z grid interval closest to the indicated points and within $0.025 \leq x \leq 0.027$.

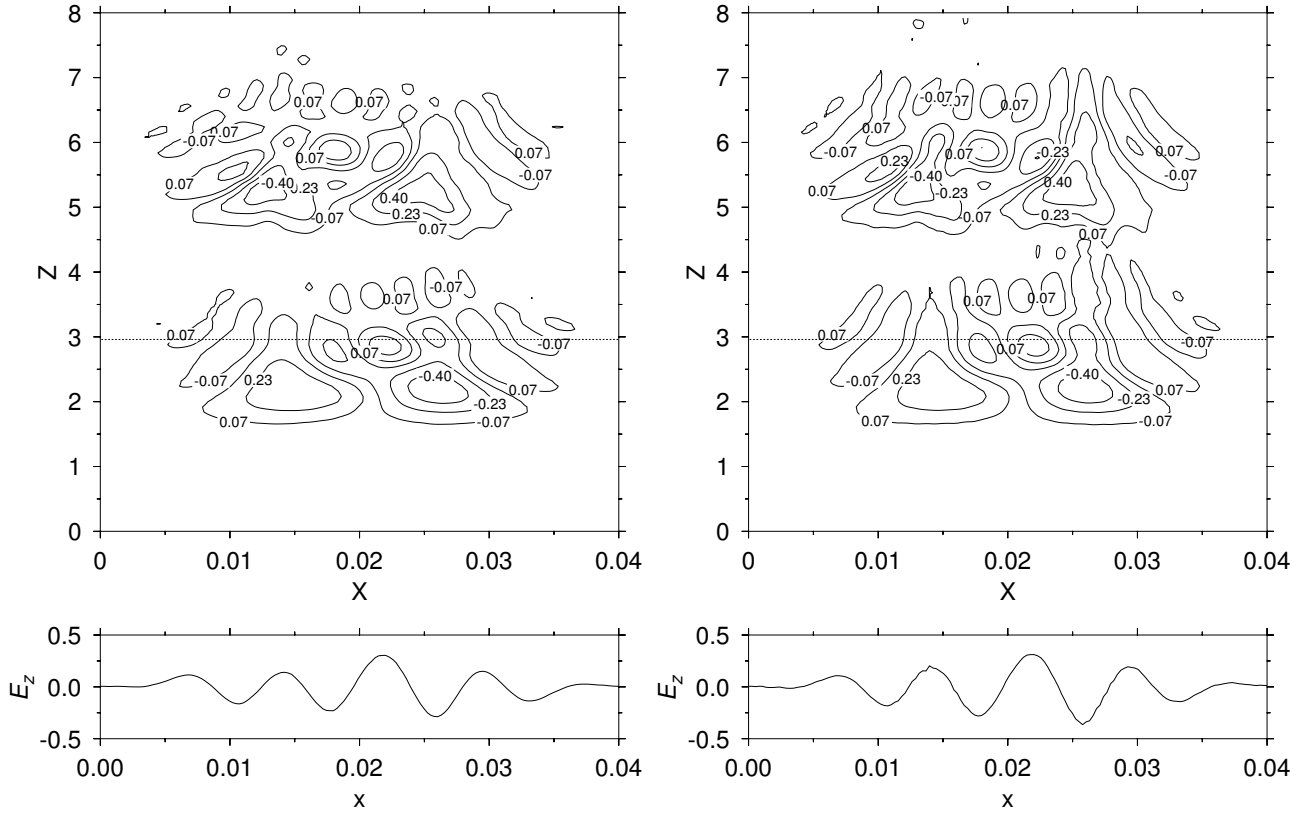


Figure 9. Contours of parallel electric field from the simulation (left) and that calculated from the potential ϕ (right) at $t = 0.009$ for $L_x = 25$ km case. Bottom: Slices of E_z as a function of x at $z = 2.96$ (indicated by dotted line in the corresponding contour plot).

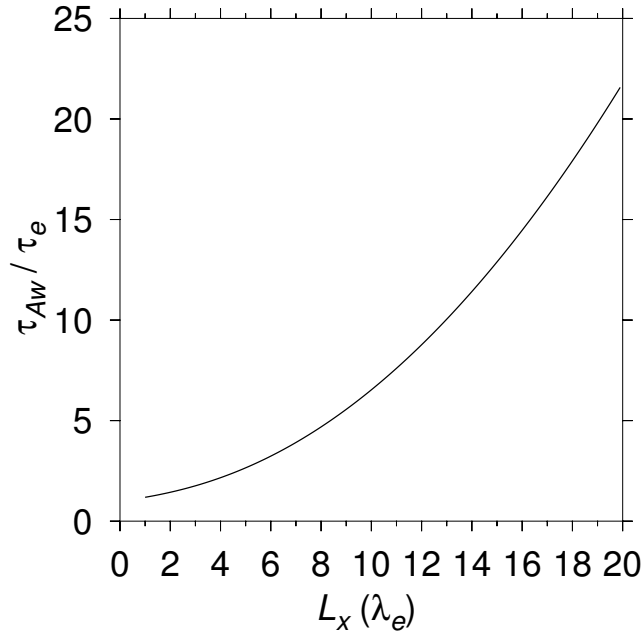


Figure 10. Ratio of Alfvén time scale (τ_{Aw}) to the electron transit time scale (τ_e) as a function of L_x where τ_{Aw} was calculated from expression (17) using $k_x = \frac{2\pi}{L_x}$.

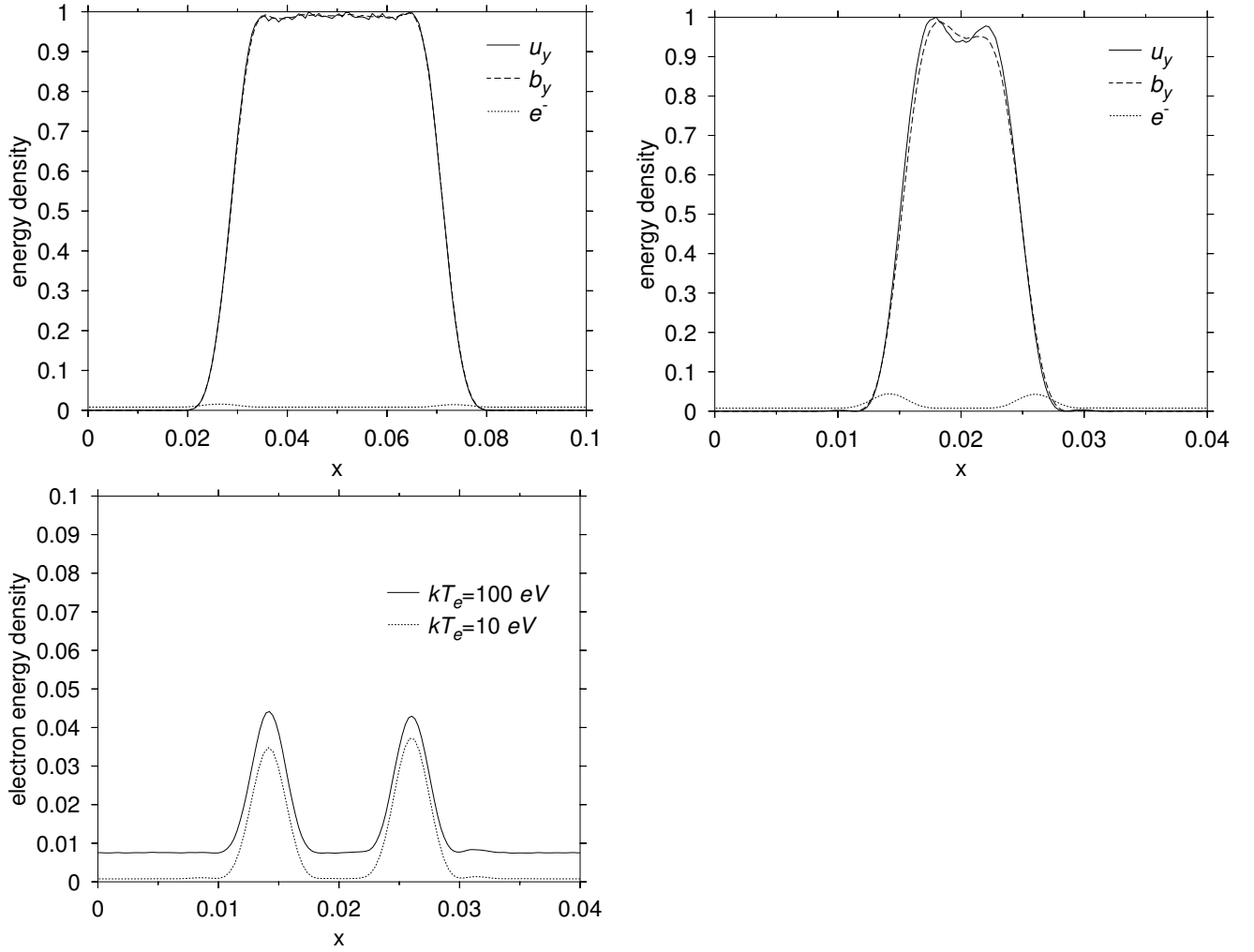


Figure 11. Top: Slices of the components of energy density at $z = 2.96$ for the $L_x = 100$ km case (left) and the $L_x = 25$ km case (right). The densities are normalized so that the maximum energy density in u_y is 1. Bottom: Electron energy density for the $L_x = 25$ km case and initial maxwellian distribution function with $kT = 100$ eV (solid line) and $kT = 10$ eV (dotted line).

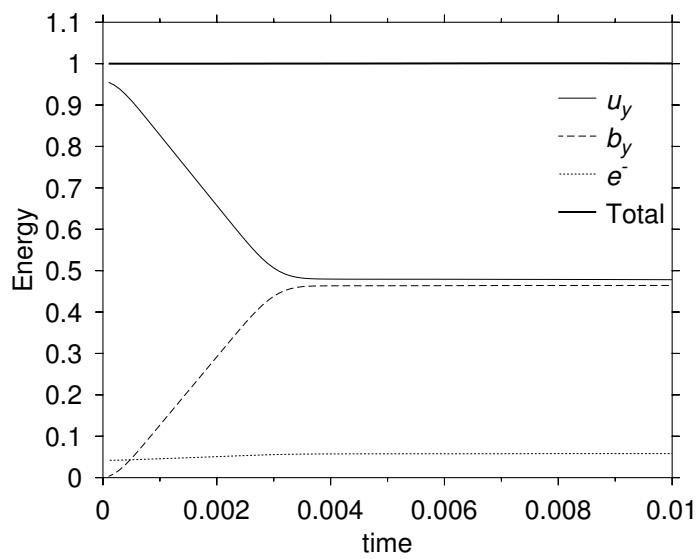


Figure 12. Energy as a function of time for the $L_x = 25$ km case.